Available online at www.sciencedirect.com
SCIENCE DIRECT®
Composites Science and Technology 65 (2005) 1098–1106
COMPOSITES SCIENCE AND TECHNOLOGY
www.elsevier.com/locate/compscitech

Damage detection of C/C composites using ESPI and SQUID techniques

Hiroshi Hatta [a,*], Mohamed S. Aly-Hassan [a], Yoshimi Hatsukade [b], Shuichi Wakayama [c], Hiroshi Suemasu [d], Naoko Kasai [e]

[a] *The Institute of Space and Astronautical Science, Japan Aerospace Exploration Agency, 3-1-1 Yoshinadai, Sagamihara, Kanagawa 229-8510, Japan*
[b] *Department of Ecological Engineering, Toyohashi University of Technology, Tempaku, Toyohashi 441-8580, Japan*
[c] *Department of Mechanical Engineering, Graduate School of Engineering, Tokyo Metropolitan University, Minami-Ohsawa, Hachioji, Tokyo 192-0397, Japan*
[d] *Department of Mechanical Engineering, Sophia University, 7-1 Kioi-cho, Chiyoda-ku, Tokyo 102-8554, Japan*
[e] *Nanoelectronics Research Institute, AIST, 1-1-1 Umezono, Tsukuba, Ibaraki 305-8568, Japan*

Received 7 November 2003; received in revised form 1 November 2004; accepted 23 November 2004
Available online 20 January 2005

Abstract

Three non-destructive evaluation (NDE) techniques, Acoustic Emission (AE), Electronic Speckle Pattern Interferometry (ESPI), and Superconducting Quantum Interference Device (SQUID) current mapping, were examined for use in the damage detection of carbon–carbon composites (C/Cs). These methods were applied to observe the fracture processes of two-dimensionally-laminated (2D) and three-dimensionally reinforced (3D) carbon/carbon (C/C) composites using compact tension and double-edge-notched geometry. The fracture processes of the C/Cs were complicated and were divided into different fracture steps. The AE technique was useful to distinguish between these fracture steps. ESPI was shown to be effective at identification of small-scale delamination of the 2D-C/Cs occurring before the ultimate tensile failure. On the other hand, SQUID current mapping clearly indicated fiber failure, even in cases involving local fiber fracture.

Keywords: B. Fracture; C. Crack; D. Optical microscopy; Carbon/carbon composites

1. Introduction

Carbon/carbon composites, C/Cs, have received attention as potential high-temperature materials for advanced applications. C/Cs exhibit superior properties especially at elevated temperatures, i.e., high performance is generally enhanced with increasing temperature up to 2000 K [1–3]. High fracture toughness is one important advantage of C/Cs [4]. However, C/Cs have never been applied for use as load-bearing primary structures. This is mainly due to a lack of reliability. To attain better reliability, it is important to gather mechanical data and to establish non-destructive evaluation (NDE) techniques. It is, however, well known that the detection of damage in C/Cs using traditional techniques (e.g., ultrasonics and X-ray) is extremely difficult to carry out [5–12], mainly due to the strong attenuation of these waves in carbon materials in cooperation with complicated defects dispersed in C/Cs. Thus, effective NDE techniques should be explored in more detail.

In the present study, two rather new non-destructive techniques, Electronic Speckle Pattern Interferometry (ESPI) [13] and Superconducting Quantum Interference

* Corresponding author. Tel.: +81 427 59 8293; fax: +81 427 59 8532/8461.
E-mail addresses: hatta@pub.isas.ac.jp, hatta@pub.isas.jaxa.jp (H. Hatta).

0266-3538/$ - see front matter © 2005 Elsevier Ltd. All rights reserved.
doi:10.1016/j.compscitech.2004.11.017

Device (SQUID) gradiometry [14], as well as a conventional technique, Acoustic Emission (AE), were examined for use in the detection of damage in C/Cs. Emphasis in the present discussion was placed upon the identification of types of damage, which is difficult using more conventional techniques. In Section 2, following an explanation of materials and procedures used to induce damage in the C/Cs, ESPI and SQUID techniques are briefly reviewed; the experimental protocol is then explained. The experimental results and discussion are given in Section 3. The general conclusions are stated in Section 4.

2. Experimental procedure

2.1. Materials

Two-dimensionally laminated (2D) C/C and three-dimensionally reinforced (3D) C/C with pre-cracks were loaded, and induced damage near the notches was inspected by several NDE techniques. The mechanical properties of the C/Cs used here are summarized in Table 1.

The 2D-C/C was a cross-ply-laminated type and was reinforced with a high-modulus carbon fiber, Torayca® M40 (Toray Industries Inc., Japan). This C/C was produced via a preformed yarn method (Across Co. Ltd. Japan) [15]. This method makes use of preformed yarns, bundles of the carbon fibers (6kf) with matrix powders (coke and bulk mesophase pitch powders) dispersed within them, and with thin nylon film sheathed over. In the C/C fabrication process, the preformed yarns are first arranged unidirectionally and then are stitched together with thin nylon filament to produce an aligned preformed sheet. Then, in the present case, these sheets were laminated (crossed over each other) into a symmetric cross-ply stacking sequence to form green cross-ply C/Cs. Finally, the green body was hot-pressed in a mold at 873 K for carbonization, followed by heat treatment at a temperature of 2273 K in an inert environment. The fiber volume fraction of the 2D-C/C was 50%.

The 3D-C/C was produced by IHI Aerospace Co. Japan, and was reinforced with PAN-based fibers with a fiber volume fraction of 48%. In order to realize 3D reinforcement, a 3D fabric was used, in which z-fiber bundles were first arranged without weaving and the x- and y-fiber bundles were woven around the straight z-fiber bundles. The resulting fabric had a micro-texture, as shown in Fig. 1(a), with fiber volume fractions in the x, y, and z directions equal to approximately 16%. This fabric was then densified by a repeated hot isostatic pressure (HIP) process under pressures of >500 atm., where the impregnation material was a coal tar pitch. The final density of the 3D-C/C was 1.94 g/cm^3. Mechanical tests were performed in the z direction.

2.2. Fracture toughness measurement

In order to observe the crack extension behavior of the C/Cs, fracture toughness tests using compact tension (CT) specimens and double edge-notched (DEN) speci-

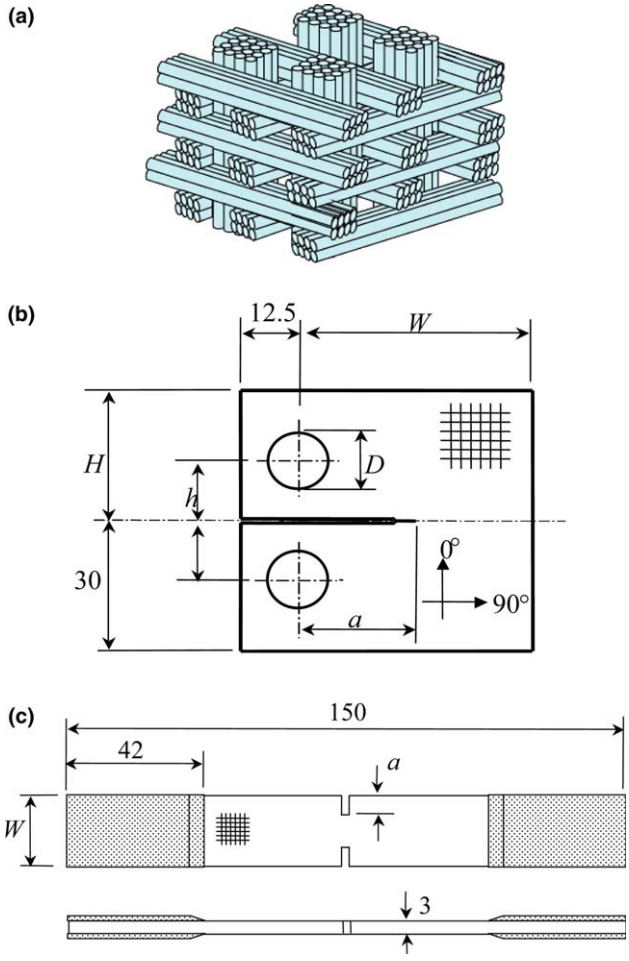

Fig. 1. Reinforcing pattern of 3D-C/C (a) and geometry of compact tension, CT (b), and double edge-notched, DEN, specimens (c).

Table 1
Properties of examined 2D and 3D C/C composites

Material	Tensile strength (MPa)	Shear strength (MPa)	Young's modulus (GPa)	Shear modulus (GPa)	Poisson's ratio	Density (g/cm^3)	Fiber volume fraction
2D-C/C	180	32	90	5.4	0.026	1.69	0.5
3D-C/C	225	17	85	1.5	0.030	1.94	0.48

mens were performed using a screw-driven mechanical testing machine (Autograph AG-5000G, Shimadzu Corp., Japan) under a cross-head speed of 0.1 mm/min. The configurations of the CT and DEN specimens are given in Fig. 1(a) and (b). The dimensions of the CT the specimens were varied depending on the material and measurement. The detailed dimensions of the CT specimens are given in Table 2, in which t is the thickness of specimen. The pre-cracks in the CT and DEN specimens were introduced at first by a diamond wheel with a thickness of 0.4 mm, and then the notch tip was sharpened using a razor blade to achieve a size of 0.1 mm. In order to clearly observe the damage extension process during the fracture tests, the specimens were polished using diamond-paste of 15 μm diameter. The specimens were then degreased in ethanol, cleaned in an ultrasonic bath, dried at room temperature, and thinly painted white. The damage process was observed from both sides of the specimens using a traveling optical microscope at a magnification X25 and a CCD camera during the CT test. A clip gage (UB-5, Tokyo-Sokki Crop, Japan) was used to measure the crack opening displacement (COD). The detailed results and a discussion of these results are available in our previous papers [16].

2.3. Non-destructive evaluation

2.3.1. Laser speckle interferometry

Strain laser analyzer by means of electronic speckle pattern interferometry (ESPI) [13] was used for monitoring the extension of surface damage in notched C/Cs. The ESPI system used here consisted of DDS33 sensor and ISTRA 3.2 software, and was produced by Dr. Ettemeyer GmbH&Co., Germany. In the measurements, laser light (Fig. 2) illuminated the CT specimen with a working distance W_d about 240 mm. The area scanned by the strain laser analyzer was 5×8 mm^2. The reflected light was combined with a reference light provided by the same laser source. Both light waves were recorded by a high-resolution video camera and were processed into a speckle pattern by an image-processing computer. When the sample was loaded, the deformation of the sample surface produced another speckle pattern. The software produced a fringe pattern by subtracting the two different speckle patterns to determine displacement and strain distribution. The ESPI system used here

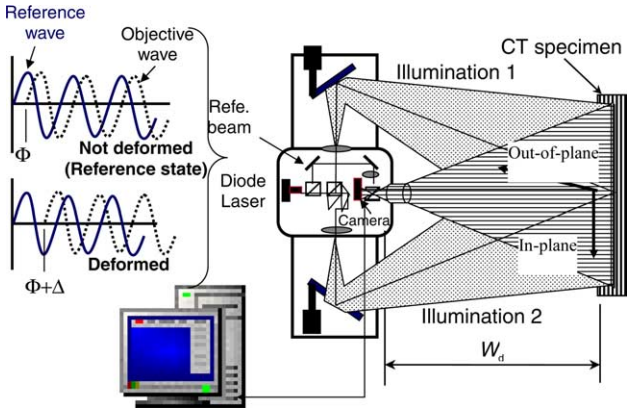

Fig. 2. Schematic drawing of an Electronic Speckle Pattern Interferometry (3D-ESPI) system.

provided a total of four illumination directions, which were combined to produce two in-plane (x, y) and an out-of-plane (z) displacement distributions.

2.3.2. Superconducting quantum interference device

The superconducting Quantum Interference Device (SQUID) is a highly sensitive magnetic sensor, which utilizes the quantum interference effect. The SQUID is more than three orders of magnitude higher in sensitivity than conventional magnetic sensors [14,17]. This high degree of sensitivity enables its application for the detection of internal and subsurface flaws in both ferromagnetic and non-ferromagnetic conducting materials [17].

Since the present study used a low-frequency current, the time-dependent term in the Maxwell equation could be neglected. In addition, the gradient of magnetic flux density (B) with respect to the z(thickness)-direction was substantially smaller than that with respect to other directions, due to the use of thin specimens. Thus, the Maxwell equation was reduced to

$$\frac{1}{\mu}\left(\frac{\partial B_z}{\partial y}\right) \approx I_x, \tag{1}$$

$$\frac{1}{\mu}\left(-\frac{\partial B_z}{\partial x}\right) \approx I_y, \tag{2}$$

where I and μ are the current density and magnetic permeability, respectively, and subscripts x and y represent the vector components. In the present experiments, a uniform electric current was injected into a specimen. Thus, defects in the C/Cs disturbed the uniform current.

Table 2
Dimensions of CT specimens

Material and test	W	D	a	h	H	t
2D C/C for ESPI & 3D C/C for SQUID	50	12.5	25	13.75	30	2D:3 3D:10
2D C/C for SQUID	100	25	50	27.5	60	3

Unit: mm.

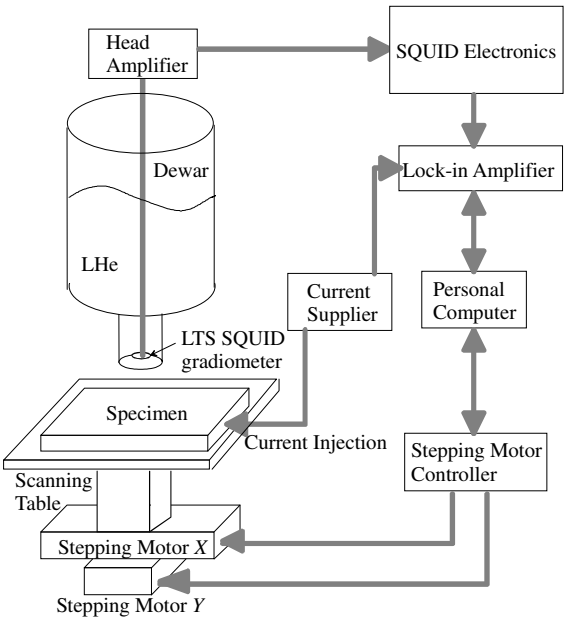

Fig. 3. SQUID–NDE system and terminal settings in a CT specimen.

Using the above equations to detect the disturbance, the defects could be identified.

An in-house low critical temperature (T_c) SQUID–NDE system, constructed in the National Institute of Advanced Industrial Science and Technology (AIST) [18,19], was used to detect damage in notched C/C composites (CT specimens, $W = 100$ mm for 2D C/Cs, $W = 50$ mm for 3D C/Cs). This system was composed of a low-T_c SQUID sensor, a planar gradiometer (pick-up coils), SQUID electronics, a helium dewar, an x–y scanning stage, and a lock-in amplifier, as shown in Fig. 3 [18,19]. A low-frequency (710 and 220 Hz for 2D C/Cs and 3D C/Cs, respectively) sinusoidal current of 90 mA was injected in the x- or y-direction into each CT specimen. Then, dB_z/dx and dB_z/dy were measured under a lift-off distance of 4.5 mm and under a sampling space of 2 mm in the x- and y-directions. Measurements were repeated after unloading in order to detect different stages of damage; undamaged and several stages of damage were assessed based on one specimen. Finally, current maps were obtained from the measured magnetic field gradients, dB_z/dy and dB_z/dx. To eliminate background noise, an unflawed copper sheet was placed beneath the CT sample.

3. Results and discussion

3.1. 2D-C/Cs

3.1.1. Microscopic observation

The microscopic observation of the CT samples demonstrated that damage growth on the surfaces of 2D-C/Cs depended on the direction of the fiber in the surface layers. For example, when the fiber direction of the surface plies in the CT samples was parallel to a pre-introduced crack (90° plies), a straight crack without fiber failure extended horizontally from the pre-notch tip, as shown in Fig. 4. On the other hand, when the fibers in the surface ply ran perpendicular to the pre-introduced crack (0° plies), the initial type of damage commonly observed during tensile loading was so-called "splitting" (Fig. 5(a)), which ran parallel to the loading direction. Splitting was defined as widely opened trans-

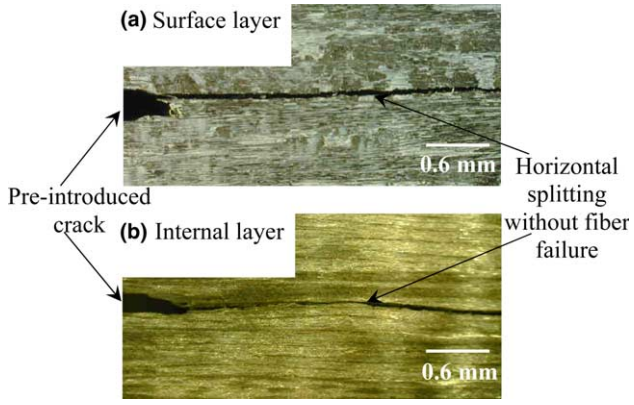

Fig. 4. Damage extension in 90° plies of a CT specimen: (a) a 90° surface ply; (b) a 90° internal ply.

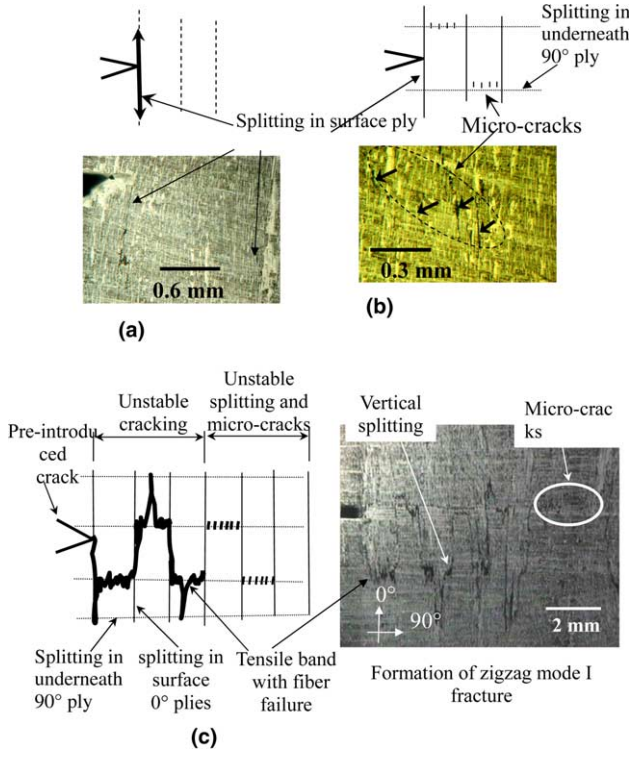

Fig. 5. Damage extension in 0° plies of a CT specimen: (a) formation of splitting; (b) formation of micro-cracks; (c) unstable zigzag crack growth.

verse cracks. The transverse cracks (TCs) [20] were induced during the cooling stage after the C/Cs were processed [21]. When the applied load was increased, the splitting of 2D-C/Cs did not grow; however many micro-cracks appeared between the splits in the 0° plies, as shown in Fig. 5(b). The micro-cracks in the 0° ply were mostly located located on the underneath splitting in the adjacent 90° ply developed from the TCs. This tendency indicated that the micro-cracks were induced by stress concentration cased by the existence of the splittings in the adjacent 90° ply. When the load was further increased, the number of micro-cracks increased, and the splitting in the surface 0° ply and the micro-cracks eventually joined to form a large crack extension, zigzag crack growth, as shown in Fig. 5(c). This extension facilitated the additional formation of splitting and micro-cracks ahead of the main crack. By repeating this process, the crack including fiber fracture extended across the ligament.

As the zigzag crack extended, the thickness of the samples expanded, as shown in Fig. 6, in which a zigzag crack propagated up to approximately 13 mm. Usually, this kind of expansion is observed in delaminated composites.

3.1.2. AE monitoring

Fig. 7 depicts the applied load and the acoustic-emission (AE) event rates as a function of crack opening displacement during the first loading cycle of a CT test. Note in this figure that multiple splitting gave rise to a non-linear load-COD relationship, and zigzag crack growth induced a rapid load drop.

The crack extension resistance (*R*-) curve was obtained based on the load-COD relationship using a compliance method [22], and the results are shown in Fig. 8. The lengths to the zigzag crack tip and to the most advanced micro-crack were tentatively used as the representative crack length. Crack extension based on a micro-crack clearly yielded a periodically fluctuating R-curve. In the first cycle, fracture resistance, based on

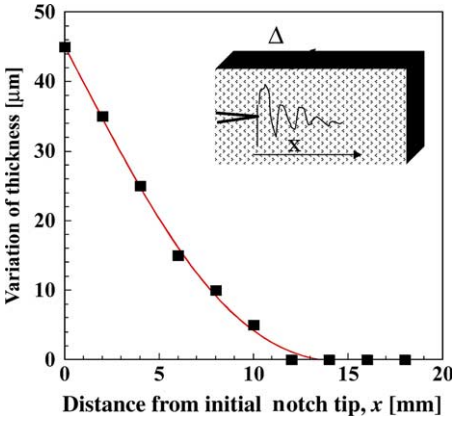

Fig. 6. Thickness increment versus distance from the initial notch tip.

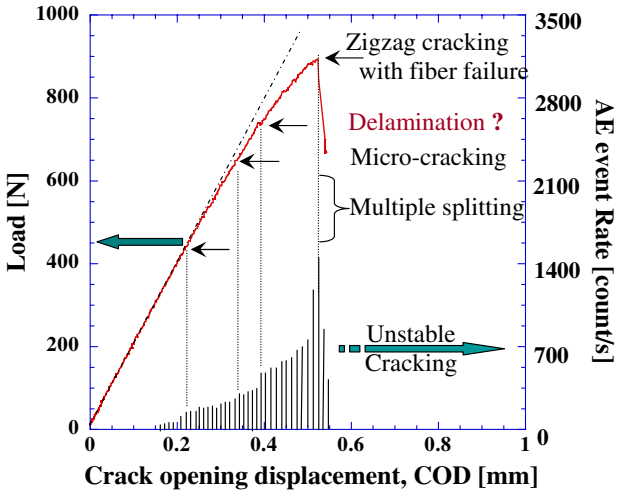

Fig. 7. Acoustic-emission (AE) event rates and load as a function of crack opening displacement for the first loading cycle of a CT test of 0°/90° C/C.

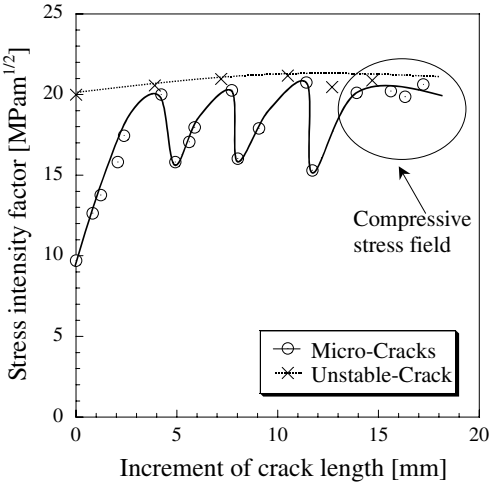

Fig. 8. Zigzag *R*-curves based on micro-cracks and unstable zigzag crack growth 0° plies as a function of increment of crack length.

the micro-crack, rapidly increased from an initiation value of 9.7 MPa $m^{1/2}$ to a maximum value of about 20 MPa $m^{1/2}$. The next and further cycles had a higher initial value than that of the first cycle. This difference between the initial values was due to the existence of splits and micro-cracks at the initial stages of subsequent cycles. When a zigzag crack front was used, the initial and saturated values were similar to the maximum value of the micro-crack *R*-curve, i.e., no rising *R*-curve was observed for a zigzag *R*-curve. This finding indicated that a rising *R*-curve, i.e., high fracture toughness, in 2D-C/Cs took place during micro-crack formation.

3.1.3. ESPI

Fig. 9 shows the typical ESPI patterns at different damage stages when the surface plies were parallel to the load direction, i.e., 0° plies. These ESPI fringe

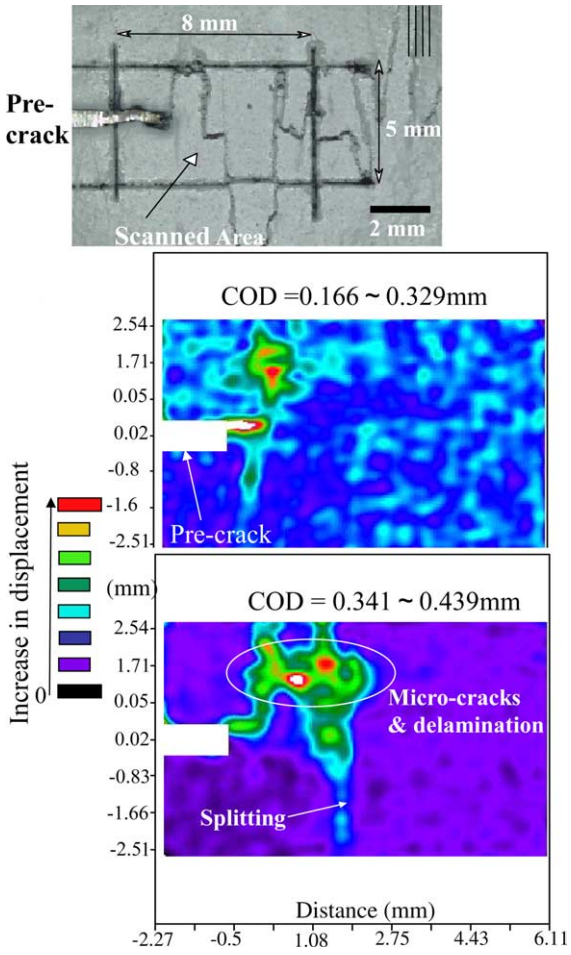

Fig. 9. Typical ESPI results on 0° ply surfaces of 2D C/Cs at CODs to monitor the damage process.

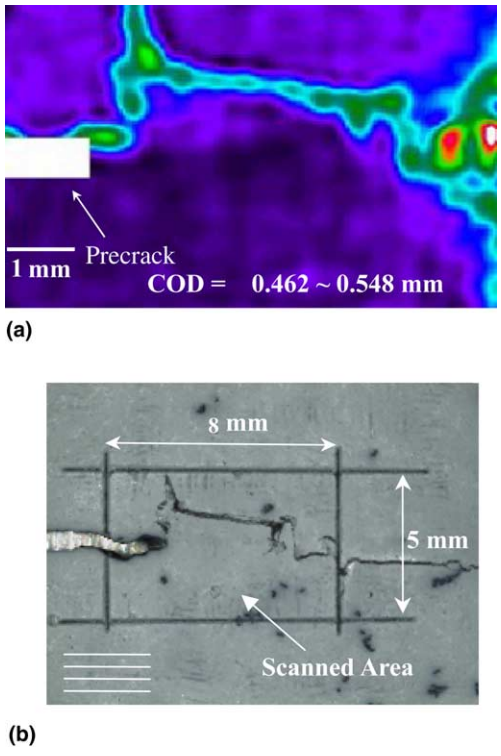

Fig. 10. Typical ESPI result on a 90° ply surface of a 2D C/C (a) and corresponding damage observed using optical microscope (b).

patterns were obtained for displacement in the z direction by subtracting two speckle patterns with two different CODs, 0.341 and 0.439 mm. These CODs were less than that of the fiber failure, as shown in Fig. 7. The upper figure shows a photograph of corresponding damage after zigzag crack had occurred. Similarly, damage in the 90° plies, when the surface plies are normal to the load direction, can be clearly observed using the ESPI fringe pattern as shown in Fig. 10(a). This pattern was obtained using different CODs, 0.462 and 0.548 mm. Fig. 10(b) is the corresponding damage at a COD of 0.548 mm. Comparing Figs. 9 and 10, it becomes evident that interlaminar debonding (delamination) tends to develop at the intersections of splits running through 0° and 90° plies, as indicated by the circles in the figures. Hence, the main conclusion of this section would be that partial delamination in 2D C/Cs occurred before zigzag crack growth took place, and delamination was clearly observed using the ESPI technique.

3.1.4. SQUID

Fig. 11(a)–(d) shows the current maps of a CT specimen obtained by the SQUID technique at the following

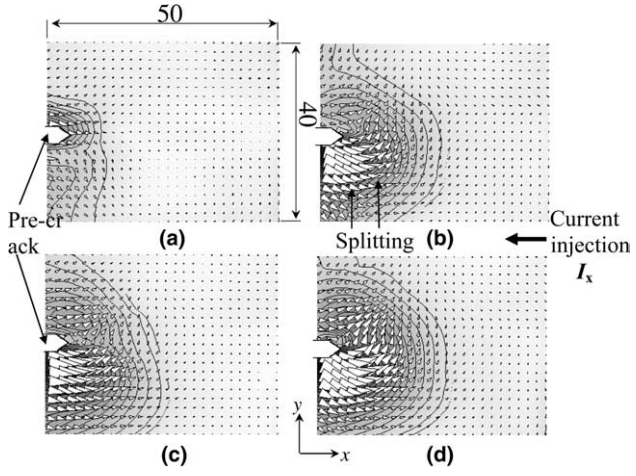

Fig. 11. Detoured current maps obtained by uniform current injection from the x-direction: (a) at the initial stage; (b) at the splitting stage; (c) at the micro-crack stage; (d) at the unstable zigzag-crack stage.

stages: (a) no damage, (b) splitting, (c) micro-cracks, and (d) unstable zigzag crack. These maps reflect the case of current injection in the minus-x direction. The magnitude and direction of the vector arrows in this figure represent the disturbed portion of the current intensity and direction from the uniform current. For example, arrows possessing minus-x components indicate a decrease in current intensity due to a defect. If splitting in the y-direction existed, currents would be expected to be directed in the plus or minus y-direction in

front of the splitting, and currents in the plus-x direction would be expected to appear at the front and rear sides of the splitting.

In Fig. 11(a), the disturbed currents in the minus-x direction appeared due to the pre-crack. The currents at the lower side of the pre-crack are supposed to be deflected due to a small transverse cracks in the 0° plies. In Fig. 11(b), the detoured current area significantly increases compared with that of the initial stage. At the stage shown in Fig. 11(b), two splits in the y-direction were observed microscopically at 4 and 8 mm from the notch tip (8 and 2 mm lengths, respectively); these splits extend only to the lower portion of the figure. The location of the longer split roughly agrees with the area in which the arrows in the minus-x and slight minus-y directions appear below the notch tip. In Fig. 11(c), the detoured current area extends slightly in the minus-y direction and the intensity of the detoured current below the pre-crack increases. This behavior is thought to be due to the formation of micro-cracks. At this load level, splitting at 8 mm was extended in length about 4 mm, and a split of 8-mm length newly appeared at 10 mm from the pre-crack tip. In Fig. 11(d), the splits at 4, 8, and 10 mm from the notch tip extended length to 20, 10, and 6 mm, respectively.

The thin lines drawn in Fig. 11 are contours with the same detoured current intensity. The minimum contours were drawn using twice the average value of the disturbed portion of currents in non-damaged area (noise) that is enough far from the pre-crack. The relationship between the area enclosed by the minimum contour and the damage stage, obtained from Fig. 11, is shown in Fig. 12(a). This damaged area increased as the stage advanced. Fig. 12(b) shows the relationship between the total current (the summation of the absolute values of detoured arrows in the area enclosed by the minimum contour, i.e., the damaged area) and the damage stage. The increase in the damaged area and total detoured current between the second and third stages was much larger than the increase between the splitting and micro-crack stages.

Fig. 13 shows the relationship between the total passing current, I_{yt} in the case of current injection to the plus-y direction. I_{yt} represents the total y component of the detoured current passing through the center line of the specimen ($y = 0$) in the region from the notch tip to 10 mm, where an unstable zigzag crack appeared. As shown in this figure, I_{yt} at the splitting stage changed slightly from that at the non-damaged stage. On the other hand, the amplitude at the micro-cracks and unstable zigzag crack stages decreased approximately 13% and 18%, respectively, from the amplitude at the non-damaged stage. Since the electric conductivity of fiber is much higher than that of the matrix [23], these large decreases are thought to correspond to fiber failure.

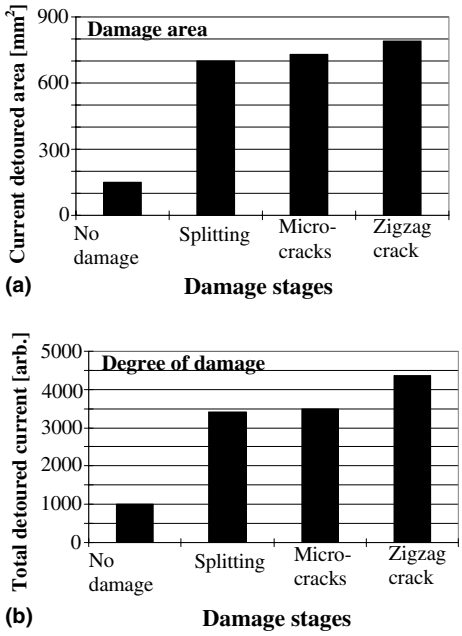

Fig. 12. The relation between the detoured current area and the stage of damage (a) and the relation between the total amount of the detoured current and the stage of damage (b).

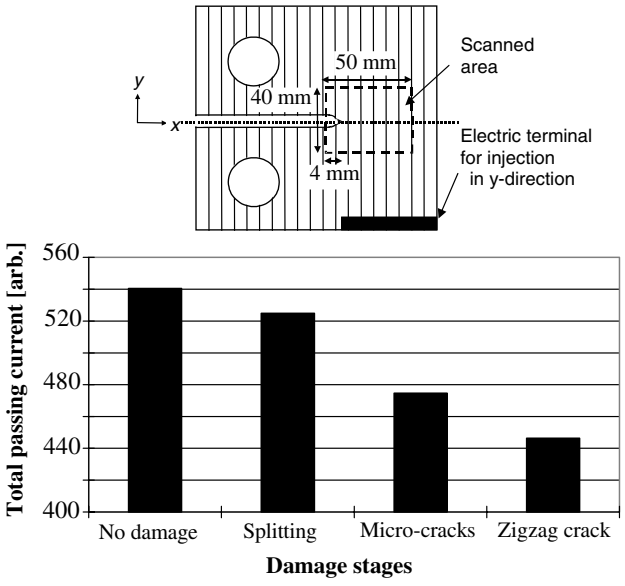

Fig. 13. The relation between the total current passing through the damaged area and the stage of damage. The upper figure illustrates the terminal setting and the scanned area. A return current pad was attached to the back of the specimen.

3.2. 3D C/Cs

3.2.1. Optical micro-observation

Fig. 14 shows the fracture pattern of the 3D C/C appearing in a DEN specimen. The initial damage that occurred during tensile loading in the CT samples

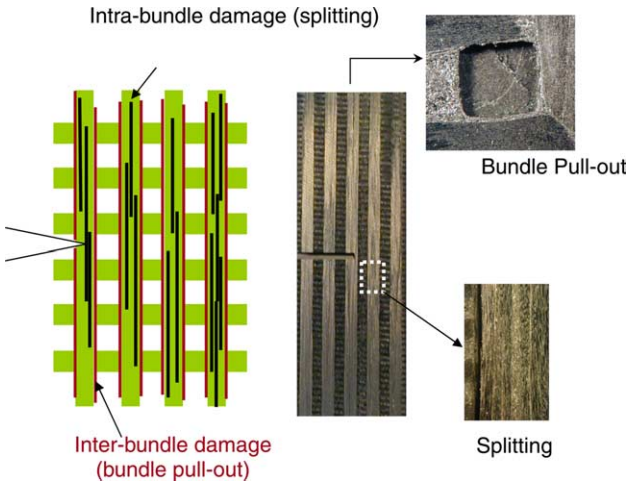

Fig. 14. Typical fracture behavior of the 3D C/C obtained by DEN tests.

of the 3D C/Cs was splitting at the bundle interfaces and within the loading bundles. This splitting could be observed even in the as-received stage and had been induced during cooling down from the processing temperatures. During loading, more splits were initiated and grew. When compared to the fracture pattern of the 2D C/C, shown in Fig. 5, the 3D C/C showed no micro-cracks, but did reveal the extension of splitting mainly due to shear stress which appeared near the crack tip. This extension of splitting was caused by extremely low interfacial strength between the fiber and matrix, and due to low shear strength of the 3D C/C [18]. Thus, the final damage observed in the DEN tests of the 3D C/Cs was pull-out of the loading bundles without any fiber failure. Moreover, in the CT tests splits arrived at the free surface. Hence, the main concern as regards damage of the 3D C/Cs should be whether or not fiber failure has occurred during the splitting process. Hence, only monitoring by the SQUID, which is effective at identifying fiber failure, was performed in the case of the 3D C/C.

3.2.2. SQUID

The relationship between the damage stages and the total passing current, I_{yt} in the 3D C/C specimen (in the case of current injection in the minus-y direction) was obtained, where the I_{yt} was the total of I_y in the region $0 < x < 10$ mm. We observed no discernible difference in the I_{yt} between the non-damaged and damaged 3D C/Cs. This result suggests that fiber fracture did not occur but large splitting did occur during the CT tests of the 3D C/C. During this process, the notch insensitivity and toughness of the 3D C/C composites could be greatly developed.

4. Conclusions

NDE techniques, Acoustic Emission (AE), Electronic Speckle Pattern Interferometry (ESPI) and Superconducting Quantum Interference Device (SQUID) current mapping, were examined in order to determine which would be effective means of evaluating C/Cs. The main conclusions obtained in this study are as follows.

1. ESPI was shown to be effective in the case of 2D C/C composites; not only splitting, micro-cracks, unstable zigzag crack extension but also partial delamination inside of the C/C were detected.
2. Partial delamination in 2D C/Cs occurred just before zigzag cracking took place. This type of delamination was induced due to stress concentrations caused by the existence of splits in 0° and 90° plies.
3. SQUID current mapping clearly demonstrated that the fracture of 2D C/Cs induced tensile fiber failure, whereas the fracture of 3D C/Cs appeared to include only a shear mode fracture without fiber failure.
4. SQUID current mapping was useful for detecting local fiber failure that was otherwise undetectable using either microscopic observations or the other NDE methods.

References

[1] Thomas CR. Essentials of carbon–carbon composites. Cambridge, England: The Royal Society of Chemistry; 1993.
[2] Savage G. Carbon–carbon composites. New York: Chapman & Hall; 1993.
[3] Fitzer E, Manocha LM. Carbon reinforcements and carbon/carbon composites. Berlin: Springer-Verlag; 1998.
[4] Schmidt DL, Davidson KE, Theibert S. Unique applications of carbon–carbon composite materials (Part One). SAMPE J 1999;35(3):27–39. 35(4) 51–63, 35(3) 47–55.
[5] Wanner A, Rizzo G, Kromp K. In: Shah SP, editor. NATO Adv Research Workshop on toughening mechanisms in quasi-brittle materials. London: Kluwer Academic Publishers; 1991. p. 405–23.
[6] Pappas YZ, Markopoulos YP, Kostopoulos V. Failure mechanisms analysis of 2D carbon/carbon using acoustic emission monitoring. NDT&E Int 1998;31(3):157–63.
[7] Philippidis TP, Nikolaidis VN, Anastassopoulos AA. Damage characterization of carbon/carbon laminates using neural network techniques on AE signals. NDT&E Int 1998;31(5):329–40.
[8] Delpech PM, Boscher DM, Lepoutre F, Deom AA, Balageas DL. Quantitative nondestructive evaluation of carbon–carbon composites by pulsed infrared thermography. NDT&E Int 1996;29(6):395–6.
[9] Coindreau O, Vignoles G, Cloetens P. Direct 3D microscale imaging of carbon/carbon composites with computed holotomography. Nucl Instrum Meth Phys Res B 2003;200:308–14.
[10] Dobiáová L, Star V, Glogar P, Valvoda V. X-ray structure analysis and elastic properties of a fabric reinforced carbon/carbon composite. Carbon 2002;40(9):1419–26.

[11] Douarche N, Rouby D, Peix G, Jouin JM. Relations between X-ray tomography, density and mechanical properties in carbon/carbon composites. Carbon 2001;39(10): 1455–65.
[12] Samah A, Paulmier D, Mansori ME. Damage of carbon–carbon composite surfaces under high pressure and shear strain. Surf Coat Tech 1999;120-121:636–40.
[13] Jones R, Wykes C. Holographic and speckle interferometry. Cambridge: Cambridge University Press; 1989.
[14] Jenks WG, Sadeghi SSH, Wikswo JP. SQUIDs for nondestructive evaluation. Physica D 1997;30:293–323.
[15] Chang T, Nakagawa T, Okura A. Studies on a new manufacturing process of carbon fiber reinforced carbon matrix (C/C) composites. Rep Inst Ind Sci 1991;35(8):1–20.
[16] Aly-Hassan MS, Hatta H, Wakayama S, Watanabe M, Miyagawa K. Comparison of 2D and 3D carbon/carbon composites with respect to damage and fracture resistance. Carbon 2003;41:1069–78.
[17] Krause HJ, Kreutzbruck MV. Recent developments in SQUID NDE. Physica C 2002;368(1–4):70–9.
[18] Hatsukade Y, Kasai N, Kurosawa M, Kawai R, Takashima H, Kojima F, et al. Detection of internal cracks and delamination in carbon-fiber-reinforced plastics using SQUID-NDI system. Physica C 2002;372-376(Part 1):267–70.
[19] Hatsukade Y, Aly-Hassan MS, Kasai N, Takashima H, Hatta H, Ishiyama A. SQUID-NDE method on damaged area and damage degree of defects in composite Materials. IEEE Trans on Appl Supercond 2003;13(2):207–10.
[20] Kogo Y, Hatta H, Kawada H, Machida T. Effect of stress concentration on tensile fracture behavior of carbon–carbon composites. J Comput Mater 1998;32(13):1273–94.
[21] Hatta H, Shibuya K, Nishiyama Y, Kogo Y. Gas leakage analysis through C/C composites. Carbon 2003;41:2381–838.
[22] Aly-Hassan MS, Hatta H, Wakayama S. Effect of zigzag damage extension mechanism on fracture toughness of cross-ply laminated carbon/carbon composites in printing. Adv Compos Mater 2003;12(2-3):223–36.
[23] Morozowski S. Semiconductivity and diamagnetism of polycrystalline Graphite nd condensed ring systems. Phys Rev 1952;85:609–20.